Dynamic reconstruction for digital tomosynthesis: A phantom proof of concept for breast care

Matteo Barbieri, Clément Jailin, Laurence Vancamberg, Stéphane Roux

Dynamic reconstruction for digital tomosynthesis: A phantom proof of concept for breast care

Matteo Barbieri[1,2], Clément Jailin[1,2], Laurence Vancamberg[1] and Stéphane Roux[2]

[1] GE HealthCare, Buc, France

[2] Université Paris-Saclay, CentraleSupélec, ENS Paris-Saclay, CNRS LMPS – Laboratoire de Mécanique Paris-Saclay, Gif-sur-Yvette, France

E-mail: matteo.barbieri@gehealthcare.com

Abstract.

Objective: Digital tomosynthesis (DTS) is a type of limited-angle Computed Tomography (CT) used in orthopedic and oncology care to provide a pseudo-3D reconstructed volume of a body part from multiple X-ray projections. Patient motion during acquisitions results in artifacts which affect screening and diagnostic performances. Hence, accurate reconstruction of moving body parts from a tomosynthesis projection series is addressed in this paper, with a particular focus on the breast. The aim of this paper is to assess the feasibility of a novel dynamic reconstruction technique for DTS and evaluate its accuracy compared to an available ground truth.

Approach: The proposed method is a combination of a 4D dynamic tomography strategy leveraging the formalism of Projection-based Digital Volume Correlation (P-DVC) with a multiscale approach to estimate and correct patient motion. Iterations of two operations are performed: i) a motion-corrected reconstruction based on the Simultaneous Iterative Reconstruction Technique (SIRT) algorithm and ii) a motion estimation from projection residuals, to obtain motion-free volumes. Performance is evaluated on a synthetic Digital Breast Tomosynthesis (DBT) case. Three slabs of a CIRS breast phantom are imaged on a Senographe Pristina™, under plate-wise rigid body motions with amplitudes ranging up to 10 mm so that an independent measurement of the motion can be accessed.

Results: Results show a motion estimation average precision down to 0.183 mm (1.83 voxels), when compared to the independent measurement. Moreover, an 84.2% improvement on the mean residual error and a 59.9% improvement on the root mean square error (RMSE) with the original static reconstruction are obtained.

Significance: Visual and quantitative assessments of the dynamically reconstructed volumes show that the proposed method fully restores conspicuity for important clinical features contained in the phantom.

Keywords: Digital tomosynthesis, Dynamic tomosynthesis, Dynamic reconstruction, 3D motion estimation, Digital Breast Tomosynthesis

1. Introduction

Digital tomosynthesis (DTS) is a type of limited-angle Computed Tomography (CT) used in the medical field to provide pseudo-3D images for screening and diagnostic purposes. However, due to the smaller number of available radiographs (9-60) and limited gantry angle (25° to 40°) [17], DTS provides lower depth resolution than CT while limiting patient radiation dose and cost. The technology has rapidly evolved in the last three decades [16, 17] and has demonstrated clinical benefits in breast [24, 50, 52], thoracic [3, 20, 32] and orthopedic [9] care by reducing the tissue superimposition issue observed in 2D radiographs.

Nevertheless, the top patient-related artifact in both CT [12, 42] and DTS [21, 31] is caused by motion during examination. Patient's motion causes blurring or replication of structures in the reconstructed volumes which may prevent radiologists from identifying clinically relevant features [29]. For instance, Vikgren *et al* [54] showed that lesions as large as 17 mm were missed in patients with breathing motion artifacts in thoracic DTS.

Since motion-pollution is a well known limitation in CT and DTS imaging, various strategies have been developed to milder its impact. Some approaches aimed at removing the motion by performing simultaneous multiple source X-ray acquisitions [6, 7, 45] or by synchronizing acquisition rate with an external physiological signal like the heartbeat or breathing cycles. [33, 39] However, these strategies significantly increase the complexity of the imaging device and protocols. Similarly, retrospective projection binning (4D-CBCT) [34, 40] was introduced in CT and extended to DTS [60] to provide easier access to the phases of a given periodic motion. In some cases a motion estimation was performed in CT between multiple phases to access a global kinematic description and motion-free reconstruction. [8, 34] However, this approach consists in performing multiple CTs (or DTS), which increases radiation dose and examination time.

Other strategies that do not rely on multiple sources hardware, external signal inputs or multiple acquisitions were developed to dynamically estimate the motion in 2D and 3D and provide a motion-free reconstructed volume from a unique series of projections. These methods are the focus of our state of the art.

Concerning pure 2D methods applied to CT, estimation of in-plane motion is performed on raw projection data in CT by different means such as interpolation between successive helical fan-beam frames, [55] correlation between successive spectral moments of the projections [44, 57] or cross-correlation between successive projections. [18] Approximate motion corrections in the projection space were then implemented before feeding the corrected projections to the standard reconstruction algorithm.

Other 2D/3D hybrid methods estimate the 3D positions of some physical [37] or fiducial [13, 14] landmarks, reproject them and apply 2D transformations (rigid or non-rigid) to the projections to minimize the distance between the original landmarks and their reprojected positions. As previously, the corrected projections are used as input of a reconstruction algorithm. For DTS, a method similar to [37] has been used to highlight the presence of patient's motion in Digital

Breast Tomosynthesis (DBT), [47] and led to a U.S. Patent in 2021. [43] Indeed, since a standard 45 mm breast a DBT examination is longer than a standard Digital Mammography (9s vs. 1s), motion artifacts in DBT have a higher impact and must be detected and tackled.

More recently, it was acknowledged that a 2D correction of a 3D motion was not sufficient and methods to include 3D kinematics in the reconstruction process from a single routine scan were developed. First attempts were made analytically on a motion-compensated Filtered Back-Projection (FBP) [13] but were limited to the correction of RBMs. This nevertheless enabled Choi *et al* to estimate 3D RBMs by minimizing the difference in the projection space of fiducial landmarks and their reprojection from the current status of the reconstructed volume. Later on, Motion-compensated SART (McSART) [11, 48] enabled further development in non-rigid 3D motion estimation. In fact, it enabled the development of other dynamic iterative methods relying on an estimation of 3D kinematics minimizing the projection residuals — defined as the norm between the original projections and reprojection of the related motion-corrected volume — such as the Simultaneous Motion Estimation and Image Reconstruction (SMEIR) [56] or Projection-based Digital Volume Correlation (P-DVC) reconstruction [27, 28] algorithms. In the latter, the principle is to exploit a linearization of the dynamic reconstruction problem and to iteratively update a motion corrected reconstruction with the estimated kinematic fields extracted by Gauss-Newton minimization over a large kinematic basis.

Finally, the development of artificial intelligence tools applied to the medical field showed good reconstruction performances and was used for the purpose of dynamic reconstruction. [25, 35, 36] However, training of such tools requires ground truth information which is hardly accessible in tomosynthesis due to the specific geometry and ill-conditioning of the inverse problem. Application of these methods to DTS are still a challenge for reconstruction but may be tackled in a near future. [46]

Considering options suited to the present use case, *i.e.,* based on a single series of projections, only some strategies exploiting the tracking and registration of physical landmarks (bright spots in projections) are available but need to be adapted to the specific case of tomosynthesis. In this respect, the technique used in Marchant et al. [37] was implemented and used as a baseline for comparison in the following.

This paper describes a dynamic reconstruction framework which uses the P-DVC formalism from [28] to estimate motion and an iterative algebraic motion-compensation reconstruction based on the Simultaneous Iterative Reconstruction Technique (SIRT) algorithm to correct the volumes. The originality of this work, in the context of DTS reconstruction, lies in its ability to both identify non-rigid 3D motion and produce a motion-free volume from a single routine scan without the need for predictable motion, dedicated hardware, or changes to existing clinical procedures. For this purpose, a novel general method is presented and thoroughly evaluated through a detailed experimental setup. Since breast imaging is by far the main use application of tomosynthesis, a widely used breast imaging phantom is selected to represent a reasonable texture and provide

access to independent motion measurements. Evaluation is then performed both quantitatively and qualitatively.

The paper is organized as follows: Section 2 presents the Digital Breast Tomosynthesis framework and the data used for experimental validation. The proposed method for the motion-compensated reconstruction and kinematic estimation are presented in a general form in section 3 with highlights specific to the breast phantom application case are detailed in 3.3. The results of dynamic reconstruction experimental validation are presented in section 4 and further discussed in section 5.

2. Breast phantom application data

Since breast care is the principal use case for DTS, the choice was made to apply the dynamic tomosynthesis method to Digital Breast Tomosynthesis (DBT). In this section, a brief introduction to tomosynthesis is presented and the acquisition protocols used for the breast application case are described.

2.1. Digital Breast Tomosynthesis (DBT) acquisition system

The validation of the proposed method was performed using a Senographe Pristina™ (GE HealthCare, Chicago, IL, USA) Digital Breast Tomosynthesis system. In this system, the X-ray source performs a step-and-shoot routine along a circular arc above a fixed detector plane of size $n_\xi \times n_\eta = 2394 \times 2850$ pixels (pitch of 0.1 mm) and acquires $n_\theta = 9$ cone-beam radiographs at angles $\{\theta_i\}_{i\in[\![1,n_\theta]\!]}$ equally distributed between -12.5° and 12.5°. The air gap between the detector and the top of the patient support is of 23.24 mm, the source rotation center is at a distance of 43.24 mm from the detector and the rotation radius is 616.76 mm long. In the present experiment, all radiographs are corrected by an angle-wise flatfield acquired beforehand and the terminology *projection* refers to the flatfield-corrected and negative-log-transformed radiographs.

To identify the geometry, two orthonormal frames are defined $\boldsymbol{X} = \{x, y, z\}$ and $\boldsymbol{\Xi} = \{\xi, \eta\}$ which respectively pave the volume and detector plane. Finally, let $(n_x \times n_y \times n_z)$ be the reconstructed volume size in voxels.

2.2. Breast phantom acquisitions

In this study, the aim is to synthetically generate a motion-polluted projection series from several motionless acquisitions. A stack of three, 10 mm thick, plates of the BR3D Breast Imaging phantom model 020 (CIRS Inc., Norfolk, VA, USA), [15] was used for the experimental validation of the proposed algorithm. Each plate contains a swirled pattern of tissue-equivalent adipose and glandular materials mimicking breast texture and additional fibers, spheroidal masses and microcalcification-like specks are present in one plate providing finer details. Finally, small copper markers were manually pinned on the boundaries of each phantom plate to provide additional landmarks.

To generate the synthetic motion-polluted cases, nine motionless DBTs were performed. Between each motionless DBT, each plate of the phantom was moved independently following random in-plane Rigid Body Motions (RBM). As described in figure 1a, synthetic motion-polluted acquisitions are generated by randomly selecting projections from the nine motionless series (one projection per angle), thus mimicking a motion occurring during a DBT sweep. 30 different and independent cases were thus generated. The resulting motion, referred to as "shear motion" in the following, is thus parameterized by 9 degrees of freedom, which depict two orthogonal translations and a rotation per plate.

In addition, all nine original volumes were reconstructed and the 3D positions of the copper markers were manually extracted, providing a ground truth for the phantom configuration. Motion amplitudes were recovered by measuring the displacement of the copper markers and were found to range up to 10 mm with respect to the configuration of the 0° projection.

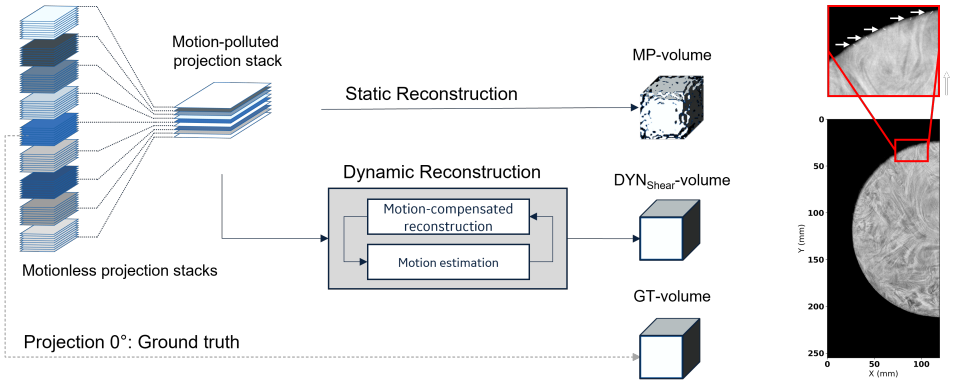

(a) (b)

Figure 1: (a) Generation of a synthetic motion-polluted case from multiple series of motionless projections and reconstruction schemes (b) Projection of the phantom with copper markers (indicated by white arrows).

3. Methods

This section describes the reconstruction method, the Projection-based Digital Volume Correlation (P-DVC) formalism and the general method for dynamic (*i.e.,* motion estimation and correction) reconstruction.

3.1. Reconstruction algorithms

3.1.1. Image formation In this work, the physical model assumes a monochromatic X-ray cone beam and non-diffracting material. From here on, $\boldsymbol{p}(\boldsymbol{\Xi}) = \{p_{\theta_i}(\boldsymbol{\Xi})\}_{i\in[\![1,n_\theta]\!]}$ of size $(n_\theta, n_\xi \times n_\eta)$ is the vector of the projection values for all angles and $\boldsymbol{\Pi} = \{\Pi_{\theta_i}\}_{i\in[\![1,n_\theta]\!]}$ of size $(n_\theta, n_x \times n_y \times n_z, n_\xi \times n_\eta)$

the associated projection operator. The flatfield correction is performed with a method adapted from [26].

3.1.2. Static reconstruction The reconstruction algorithms used in tomosynthesis are similar to those used for CT imaging, notwithstanding the difference in angle coverage. The main solutions are algebraic such as ART [23], SIRT, [22] and SART [2] or analytic such as the Filtered Back-Projection algorithm. [19, 30] Since algebraic methods are known to perform better on limited-angle problems [40], and because of the limited number of available projections, the SIRT algorithm is used in the present study.

Let ψ be a vector representing any given 3D volume, the reconstruction in tomosynthesis is sought as f, a value of ψ minimizing the "projection residual" L2 norm, given a positivity constraint

$$f = \underset{\psi>0}{\text{Argmin}} \sum_{i=1}^{i=n_\theta} \left\| p_{\theta_i}(\boldsymbol{\Xi}) - \Pi_{\theta_i}[\psi(\boldsymbol{X})](\boldsymbol{\Xi}) \right\|^2 . \tag{1}$$

By denoting f^n the solution at iteration n, the general formulation of the SIRT algorithm is given by

$$f^{n+1}(\boldsymbol{X}) = f^n(\boldsymbol{X}) + \lambda \sum_{i=1}^{i=n_\theta} C_{\theta_i} \Pi_{\theta_i}^\top R_{\theta_i} \left[p_{\theta_i}(\boldsymbol{\Xi}) - \Pi_{\theta_i}[f^n(\boldsymbol{X})](\boldsymbol{\Xi}) \right] \tag{2}$$

where C_{θ_i} and R_{θ_i} are diagonal matrices with $(C_{\theta_i})_{jj} = 1/\sum_l (\Pi_{\theta_i})_{lj}$, $(R_{\theta_i})_{ll} = 1/\sum_j (\Pi_{\theta_i})_{lj}$ and λ a relaxation parameter set to 1.0 in the following. In addition, the process is considered to have reached convergence if the relative improvement of the residual norm for the current iteration is lower than 10%.

3.1.3. Motion-compensated reconstruction Motion-compensated reconstruction has been effectively implemented and used in CT dynamic reconstruction frameworks such as the ones from [28, 48, 56] through a modified version of the SART algorithm. Here, a motion-compensated reconstruction based on the SIRT algorithm is preferred due to the small number of available projections.

The key for motion compensation is to ensure that numerical projections are performed with objects deformed to the state of the current time step whereas volume updates are computed in the reference state as displayed in [41, 53]. For this purpose, the update presented in (2) is transformed as follows

$$f^{n+1}(\boldsymbol{X}) = f^n(\boldsymbol{X}) + \lambda \sum_{i=1}^{n_\theta} (C_{\theta_i} \Pi_{\theta_i}^\top R_{\theta_i} [p_{\theta_i} - \Pi_{\theta_i}[f^n(\boldsymbol{X} + \boldsymbol{U}_i)]])(\boldsymbol{X} + \boldsymbol{W}_i) \tag{3}$$

where $\boldsymbol{U} = \{\boldsymbol{U}_i\}_{i \in [\![1, n_\theta]\!]}$ is the series of 3D Eulerian displacement fields for each angle θ_i and $\boldsymbol{W} = \{W_i\}_{i \in [\![1, n_\theta]\!]}$ their Lagrangian counterpart.

3.2. Motion estimation

3.2.1. Gauss-Newton scheme In the following, $f(\boldsymbol{X})$ denotes the absorption of the reconstructed volume (encoded in gray levels), $f(\boldsymbol{X}+\boldsymbol{U}_i)$ the deformed volume at the time of projection i with $\boldsymbol{U}_i = \sum_{j=1}^{N} u_{ij}\boldsymbol{\Phi}_j(\boldsymbol{X})$ the related displacement field and $\boldsymbol{\Phi}(\boldsymbol{X})$ a kinematic basis. With those notations and $\boldsymbol{V}$ representing a vector of the space containing the vector fields $\boldsymbol{V}_i$ for each projection i, the reconstruction problem presented in (1) becomes

$$(f(\boldsymbol{X}),\boldsymbol{U}) = \underset{\psi,\boldsymbol{V}}{\text{Argmin}} \sum_{i=1}^{n_\theta} \|p_{\theta_i} - \Pi_{\theta_i}[\psi(\boldsymbol{X}+\boldsymbol{V}_i)]\|^2 \ . \tag{4}$$

The problem defined by (4) is non-convex and has no ready analytic solution. However, it may be locally approximated by linearization and successive corrections $\delta\boldsymbol{U}^k$ are sought, such that $\boldsymbol{U}^{k+1} = \boldsymbol{U}^k + \delta\boldsymbol{U}^k$ where $\delta\boldsymbol{U}^k$ is a small perturbation of $\boldsymbol{U}^k$. Hence,

$$\begin{aligned} \delta\boldsymbol{U}^k &= \underset{\delta\boldsymbol{V}}{\text{Argmin}} \sum_i \|p_{\theta_i}(\boldsymbol{\Xi}) - \Pi_{\theta_i}[f^k(\boldsymbol{X}+\boldsymbol{U}_i^k) + \boldsymbol{\nabla} f^k(\boldsymbol{X}+\boldsymbol{U}_i^k)\delta\boldsymbol{V}_i](\boldsymbol{\Xi})\|^2 \\ &= \underset{\delta\boldsymbol{V}}{\text{Argmin}} \sum_i \|p_{\theta_i}(\boldsymbol{\Xi}) - \Pi_{\theta_i}[f^k(\boldsymbol{X}+\boldsymbol{U}_i^k)] - \Pi_{\theta_i}[\boldsymbol{\nabla} f^k(\boldsymbol{X}+\boldsymbol{U}_i^k)\delta\boldsymbol{V}_i](\boldsymbol{\Xi})\|^2 \end{aligned} \tag{5}$$

given the linearity of the projection. Defining $r_i(f^k,\boldsymbol{U}^k) = p_{\theta_i}(\boldsymbol{\Xi}) - \Pi_{\theta_i}[f^k(\boldsymbol{X}+\boldsymbol{U}_i^k)](\boldsymbol{\Xi})$ as the "projection residual" and $\delta\boldsymbol{V}_i = \sum_{j=1}^{N}\delta v_{ij}\boldsymbol{\Phi}_j(\boldsymbol{X})$ yields

$$\begin{aligned} \delta\boldsymbol{u}^k &= \underset{\delta v}{\text{Argmin}} \sum_i \|r_i(f^k,\boldsymbol{U}^k) - \sum_j \Pi_{\theta_i}[\boldsymbol{\nabla} f^k(\boldsymbol{X}+\boldsymbol{U}^k)\boldsymbol{\Phi}_j(\boldsymbol{X})]^\top(\boldsymbol{\Xi})\cdot\delta v_{ij}\|^2 \\ &= \underset{\delta v}{\text{Argmin}} \sum_i \|r_i(f^k,\boldsymbol{U}^k) - \sum_j S_{ij}(f^k,\boldsymbol{U}^k)\cdot\delta v_{ij}\|^2 \end{aligned} \tag{6}$$

with $S_{ij}(f^k,\boldsymbol{U}^k) = \Pi_{\theta_i}([\boldsymbol{\nabla} f^k(\boldsymbol{X}+\boldsymbol{U}^k)\boldsymbol{\Phi}_j(\boldsymbol{X})]^\top(\boldsymbol{\Xi})$ being the projected sensitivity of the kinematics described by $\boldsymbol{\Phi}_j$ at angle θ_i. Equation (6) shows that $\delta\boldsymbol{u}^k$ can be estimated by solving a least square regression problem between the projected residuals $\boldsymbol{r}(f^k,\boldsymbol{U}^k)$ and the projected sensitivities $\boldsymbol{S}(f^k,\boldsymbol{U}^k)$, which can be written

$$\delta\boldsymbol{u}^k = [\boldsymbol{S}(f^k,\boldsymbol{U}^k)^\top\boldsymbol{S}(f^k,\boldsymbol{U}^k)]^{-1}\boldsymbol{S}(f^k,\boldsymbol{U}^k)^\top\boldsymbol{r}(f^k,\boldsymbol{U}^k) \ . \tag{7}$$

Since the hessian matrix is often badly conditioned, a Tikhonov regularization parameterized by μ may be added to solve (6), which translates into

$$\delta\boldsymbol{u}^k = [\boldsymbol{S}(f^k,\boldsymbol{U}^k)^\top\boldsymbol{S}(f^k,\boldsymbol{U}^k) + \mu I_N]^{-1}\boldsymbol{S}(f^k,\boldsymbol{U}^k)^\top\boldsymbol{r}(f^k,\boldsymbol{U}^k) \ , \tag{8}$$

with I_N the identity matrix of size $N\times N$.

3.2.2. Multiscale approach A known limitation of the Gauss-Newton method is that the correction $\delta \boldsymbol{u}$ is assumed to be small. Hence, the relevance of the gradient operator is achieved for an upper bound of the expected motion amplitude ℓ by applying a 2D Gaussian filter of variance $\sigma_f = \ell$ on the projections and downsampling by retaining 1 out of $\ell \times \ell$ pixels. A first order Taylor-expansion may capture a rough estimation of the motion amplitude which can be used as a pre-correction for the major part of the motion through motion-compensated reconstruction. Then, a finer analysis can be made with a shallower filter and as ℓ decreases, successive iterations eventually allow to directly consider the unfiltered projections. This constitutes a multiscale (pyramidal) approach [1], which can prevent the occurrence of secondary minima trapping and significantly reduce computational cost.

In addition, the least-squares problem from (6) remains ill-conditioned. The Tikhonov regularization through parameter μ is a classical trick to circumvent this difficulty. The higher μ is, the stronger the limitation on poorly-determined kinematic modes. Hence, progressively decreasing μ when going through the identification iterations will gradually encompass finer motion details. At a given scale and regularization intensity the identification process is considered to have reached convergence if the relative improvement of the residual norm after reconstruction is lower than 30. The run finishes when $\ell = 1$ and $\mu = 0$.

3.2.3. Dynamic tomosynthesis algorithm Given the SIRT algorithm and its dynamic counterpart McSIRT (section 3.1), the general motion identification process is summarized in the pseudo-code algorithm 1.

The first step is the reconstruction of the polluted volume ($\boldsymbol{u}^0 = \boldsymbol{0}$) at the scale ℓ assumed to be the largest patient motion amplitude. From there, the sensitivities and the increment $\delta \boldsymbol{U}^k$ are computed and used in the subsequent motion-compensated reconstruction. This procedure is iterated until convergence condition is met. Then, all subsequent scales are considered until $\ell = 1$ is reached. For convergence purposes, it is to be noted that every reconstruction (but the first) is initialized with the result of the previous one. In the case of a scale change, the previous volume is upsampled by interpolation. Let $S(\ell \times \mu)$ be the scheduled steps of scale and regularization.

3.3. Breast phantom application

3.3.1. Kinematics modeling As mentioned in paragraph 3.2.1, the motion estimation is based on a kinematic basis $\boldsymbol{\Phi}$ which should be able to capture the motions occurring during the Digital Breast Tomosynthesis (DBT) sweep. In accordance with the experiment described in section 2.2, a set of shape functions $\boldsymbol{\Phi}$ is defined as follows to capture the "shear motion". Let $\boldsymbol{\phi}$ and $\{Z_i\}_{i \in [\![1,3]\!]}$ be defined as

$$\boldsymbol{\phi} = \begin{cases} \boldsymbol{\phi}_1 = (1,0) & \text{translation along } x\text{-axis} \\ \boldsymbol{\phi}_2 = (0,1) & \text{translation along } y\text{-axis} \\ \boldsymbol{\phi}_3 = (y,-x) & \text{rotation around origin} \end{cases}, \quad Z_i = \begin{cases} 1 & \text{if } z \in \text{plate } i \\ 0 & \text{if not} \end{cases} \tag{9}$$

Algorithm 1 Dynamic tomosynthesis algorithm

procedure DYN-RECON($\boldsymbol{p}$, $\boldsymbol{\Phi}$, $S(\ell \times \mu)$)
  $\boldsymbol{u}^0 = \mathbf{0}$
  $k = 1$
  for $\ell_s \times \mu_s$ in $S(\ell \times \mu)$ **do**
    $\boldsymbol{p}_s = \text{rescale}(\boldsymbol{p}, \ell_s)$
    while Not converged **do**
      $f^k = \text{McSIRT}(\boldsymbol{p}_s, \boldsymbol{u}^{k-1})$
      Compute kinematic update $\delta\boldsymbol{u}^k$ with regularization μ_s ▷ Equation (7)
      $k = k + 1$
    end while
  end for
  $f^k = \text{McSIRT}(\boldsymbol{p}_s, \boldsymbol{u}^{k-1})$ ▷ Update with last identification
  return f^k, u^{k-1}
end procedure

To account for the independence of the different plate motion, $\boldsymbol{\Phi}$ is given by $\boldsymbol{\Phi}_{i+3(j-1)} = \boldsymbol{\phi}_i Z_j$, thus producing a 9D kinematic basis.

Note that the shape function basis $\boldsymbol{\Phi}$ only allows motion within the xy-plane. Because the actual motion of the phantom does not include motion along the z-axis (2.2) and that the DBT setup implies a breast compression limiting the motion in that direction, the degree of freedom along z may be omitted.

3.3.2. Multiscale and regularization steps For the validation experiment, no automatic scheduling of scale and Tikhonov regularization has been developed. Hence, the empiric parameters used are reported in table 1.

	Step 1	Step 2	Step 3	Step 4	Step 5	Step 6	Step 7
ℓ	32	16	16	8	4	2	1
μ	γ_2	γ_2	γ_7	0	0	0	0

Table 1: Evolution of scale and regularization parameters during convergence, where $\{\gamma_i\}_{i\in[\![1,N]\!]}$ are the eigenvalues of the hessian ordered in descending order.

3.3.3. Projection masking The motion estimation defined in (6) is assumed to work on the whole projection data. However, motion may cause part of the sample to move in and out of the field of view during the time of the acquisition. Hence the outer parts of the projections can't be used due to the potentially missing information and are removed from the motion-identification process by applying a mask Ξ_M. Since the expected motion is of about 10 mm, the mask Ξ_M excludes 100 pixels from the borders in all directions.

3.4. Comparative analysis

A comparison is performed among 6 reconstructions methods defined bellow.
MP reconstruction: is the motion-polluted reconstruction performed following the scheme in (2) with the motion-polluted projections as input.
2D warped reconstruction: is an adaptation of the method from Marchant *et al* [37]. First, radio-opaque point-like markers are tracked in the projection space and their 3D positions are estimated. Secondly, the estimated 3D positions are reprojected and used as tie points for non-rigid projection warping. Finally, a reconstruction following the scheme in (2) is performed with the warped projections as input. For the present experiment, three visible markers were identified and used for the projection warping. Two markers were taken from the two largest calcification clusters and the third one was a visible material spot on the border.
$\mathbf{DYN_{RBM}}$-reconstruction: is a reconstruction performed following the P-DVC scheme defined in this article while using $\boldsymbol{\Phi} = \phi$, thus only including the measurement of RBMs (3 degrees of freedom).
$\mathbf{DYN_{Shear}}$-reconstruction: is a P-DVC dynamic reconstruction using the 9D-kinematic basis $\boldsymbol{\Phi}$ defined in 3.3.1
$\mathbf{MC_{GT}}$-reconstruction: is a reconstruction performed with the McSIRT algorithm. Inputs are the motion-polluted projections and the manually measured displacement fields.
GT-reconstruction: is a reconstruction performed following (2) with a motionless series of projections as input as described in figure 1a.

3.5. Evaluation criteria

Evaluation metrics were used to assess performance in the projection, volume and kinematic spaces as well as the clinical outcome.

- **Residual metrics:** The evaluation criterion for the reconstruction problem is the one presented in (4) and ensures that the identification procedure leads to a higher consistency of the solution. The residual fields will be evaluated visually and with their Root Mean Square Error (RMSE) over the areas within the mask $\boldsymbol{\Xi}_M$ (3.3.1). $\overline{\boldsymbol{r}}(f, \boldsymbol{U}) = \|\boldsymbol{p}(\boldsymbol{\Xi}_M) - \boldsymbol{\Pi}[f(\boldsymbol{X}, \boldsymbol{U})](\boldsymbol{\Xi}_M)\|_2 / \sqrt{\#(\boldsymbol{\Xi}_M)}$, with $\overline{r}_i(f, \boldsymbol{U})$ the angle-wise value.
- **Volume metrics:** The gray-level RMSE is computed with the static volume as a reference. This is computed within a mask $\boldsymbol{X}_M$ excluding the background: $\overline{\boldsymbol{R}}(f, \boldsymbol{U}) = \|f(\boldsymbol{X}_M) - f_{GT}(\boldsymbol{X}_M)\|_2 / \sqrt{\#(\boldsymbol{X}_M)}$.
- **Displacement field metrics:** To appreciate the accuracy of the displacement field estimation, the RMSE of its difference with the ground truth over the mask $\boldsymbol{X}_M$ of the object is reported. For this purpose, the displacement field estimated from the manual measurements $\boldsymbol{U}_{GT}$ is taken as a reference and the result is expressed in millimeters. $\overline{\boldsymbol{R}}(\boldsymbol{U}) = \|\boldsymbol{U}(\boldsymbol{X}_M) -$

$\boldsymbol{U}_{GT}(\boldsymbol{X}_M)\|/\sqrt{\#(\boldsymbol{X}_M)}$ is the global difference and $\overline{\boldsymbol{R}}(\boldsymbol{U}_x), \overline{\boldsymbol{R}}(\boldsymbol{U}_y)$ the value limited to the x and y directions.

- **Average mean difference of degrees of freedom:** As an additional criterion on the kinematic estimation, the average of the difference between the ground truth and the estimation is computed over all combinations of motion-polluted cases for all projection angles and degrees of freedom. This metric is named $\overline{\Delta}$ and the associated standard deviation is σ_Δ.
- **Image quality metric:** As a quantitative image quality metric, the sharpness of a region, noted s, is computed by taking the standard deviation of the voxels present over a given area.[5] This area includes the object of interest and a 1 pixel large margin.
- **Visual quality assessment:** A visual evaluation of a full reconstruction slice is performed to assess the global improvement in the reconstruction and the visibility of particular embedded texture such as masses, fibers and microcalcifications. Additional high resolution figures are provided to specifically assess the microcalcification rendering.

4. Results

In this section, the results of the dynamic reconstruction pipeline applied on the breast phantom application (2.2) are presented. An in-depth description of a single case is presented in section 4.1 while a statistical analysis on the larger set of cases is presented in section 4.2.

4.1. Single case detailed description

As a first result, figure 2 reports the evolution of the mean residual error $\overline{\boldsymbol{r}}(f, \boldsymbol{U})$ for the $\text{DYN}_{\text{Shear}}$-reconstruction. The continuous blue line shows its progress throughout reconstruction iterations while the blue dots show the update of the motion estimation. In addition, green (resp. blue) dotted lines show the change of scale (resp. regularization intensity) as described in table 1. At a given resolution and regularization intensity, $\overline{\boldsymbol{r}}(f, \boldsymbol{U})$ decreases smoothly (thanks to reconstruction iterations) and experiences sudden drops immediately after motion estimation steps. These drops are however smaller as the number of reconstruction iterations increases. When decreasing the regularization intensity — thus increasing the number of available degrees of freedom — (dotted blue lines) an increase in the convergence rate is noted until it reaches a new plateau. However, it is expected to see that the mean residual error significantly increases at each scale upsampling (green dotted lines), due to the interpolation approximation to initialize the reconstruction at the new scale.

During the dynamic reconstruction iterations, the degrees of freedom have converged towards the ones identified from the ground truth. Figure 3 reports the final identified values (blue) for each degree of freedom at each phantom plate for all projection angles with respect to the manually measured ground truth (dotted black). Per definition, the displacement at angle 0° is null as the time of the central projection is considered as the reference.

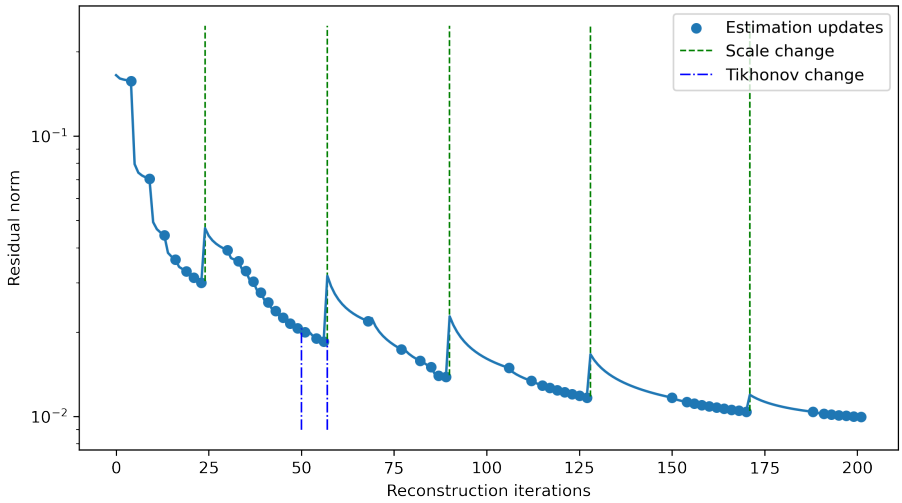

Figure 2: Residual norm of the dynamic reconstruction pipeline. Vertical green lines indicate an image scale change, vertical blue lines a Tikhonov parameter change, and blue dots indicate a motion estimation update.

Visually, the matching of the identification with the measured ground truth is excellent for the x-translation and rotations for which the maximum error is respectively 0.16 mm and 0.12°. The identification of the y-translation presents however a slight linear shift for the lower and middle plate. This shift reaches about 0.27 mm at the highest angular position of the source and will be discussed later on.

As a first visual observation, Figure 4 compares the MP-, $\text{DYN}_{\text{Shear}}$- and GT-reconstructions. It shows the projection residuals $r_{0^\circ}(f, \boldsymbol{U})(\Xi_M)$ for angle 0° clipped at ±20% of the total projection amplitude and cropped by mask Ξ_M. Visually, a strong reduction of the residual in the areas where the projection gradient is intense is striking. The discrepancies on the left phantom border and larger patterns in the object that appear in figure 4a are no longer visible in the residual of the dynamic reconstruction in figure 4b.

From the clinical point of view, it is interesting to visualize the reconstructed volumes and assess the motion artifacts. Figure 5 compares the reconstructions from a global point of view on a slice at height $z = 6$ mm. Improvement is visible from left to right and top to bottom as the kinematic models better describe the applied motion. Specifically, global intensity is restored, left phantom border becomes gradually sharper and the internal structure clearer. In addition, figure 6 displays a high resolution image of the reconstruction slices at $z = 6$ mm around 3 clusters of calcifications from the coarser (first row) to the finer ones (3rd row). Thus, it is clear that fine structures of the imaged sample are recovered by the method proposed in this paper. It is however to note that the 2D-reconstruction also displays the calcifications at the two first levels but at a

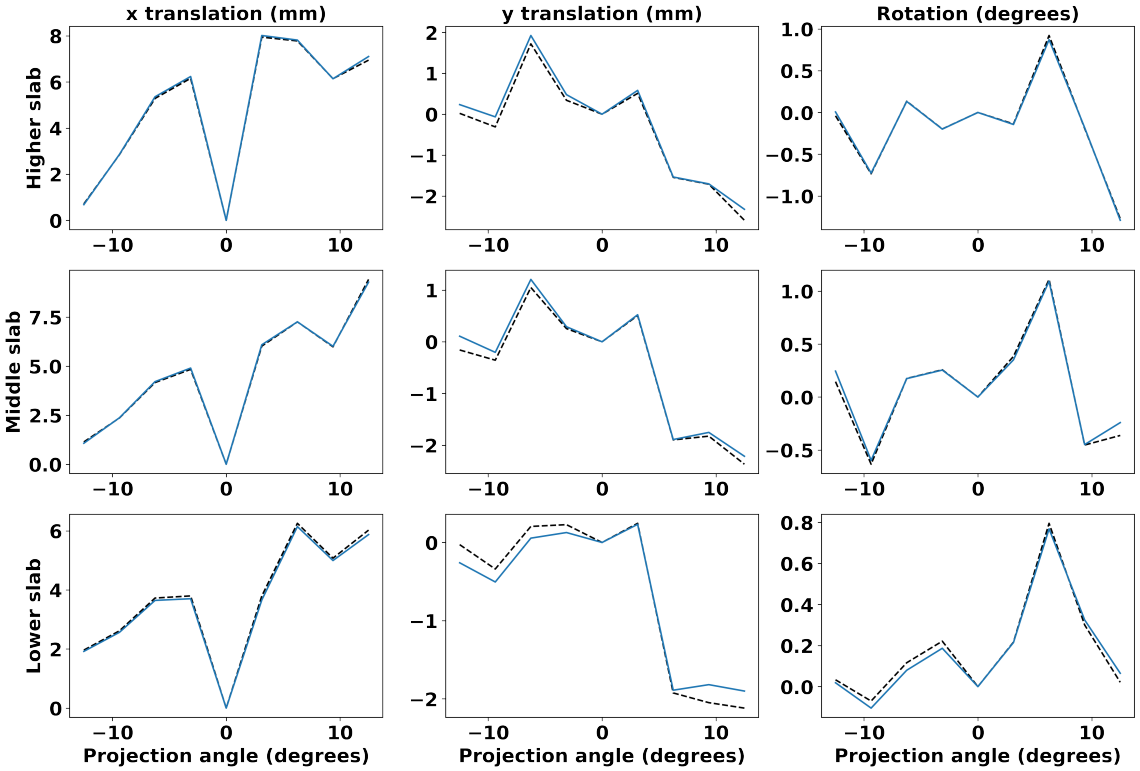

Figure 3: Identification (blue) of the 9 degrees of freedom for each phantom plate and projection angle with comparison to the measured ground truth (dotted black).

different height as the other volumes. The finer cluster is however not visible at all.

Lastly, table 2 summarizes the analytical evaluation metrics. The values of $\overline{r}(f, \boldsymbol{U})$ show that the proposed method considerably improves the consistency of the problem by a factor of 84.2%. In addition, the difference of $\overline{\boldsymbol{r}}(f, \boldsymbol{U})$ between the $\mathrm{DYN}_{\mathrm{Shear}}$- and the $\mathrm{MC}_{\mathrm{GT}}$-reconstruction is lower than the standard deviation of $\overline{\boldsymbol{r}}(f, \boldsymbol{U})$ for all static cases. Similar results can be noticed with a 96.8% improvement for $\overline{\boldsymbol{R}}(\boldsymbol{U})$ and 59.9% for $\overline{\boldsymbol{R}}(f, \boldsymbol{U})$.

4.2. Statistical analysis

A statistical evaluation of the presented method is performed on a set of 30 cases. Since all dynamic reconstructions are performed with respect to the same configuration state (the one of the projection at the angle 0°) and that the frame of the kinematic basis is fixed, for all experiments, the reconstructions are all comparable among each other.

As a first insight, the initial mean residual error $\overline{\boldsymbol{r}}(f, \boldsymbol{U})$ of the 30 motion-polluted cases is in average 1663% higher than the GT-reconstruction. As a result of the dynamic reconstruction, the

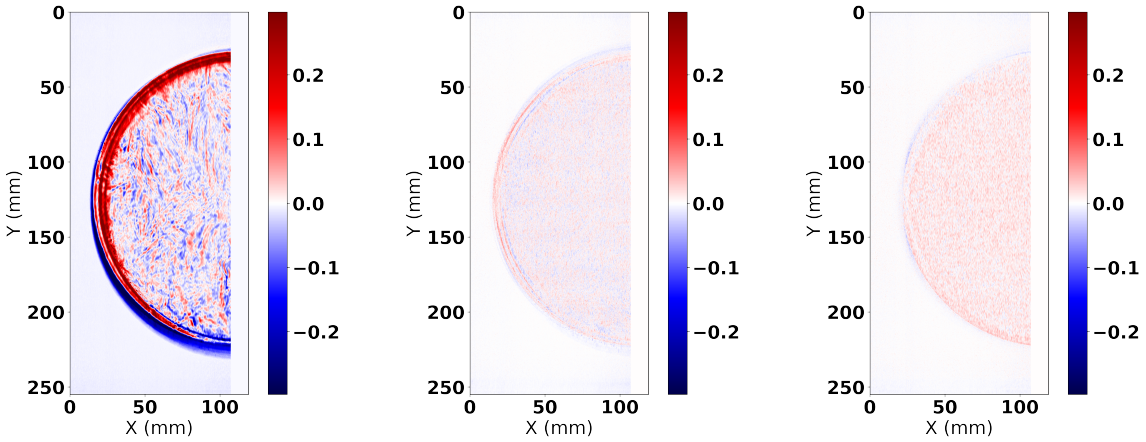

(a) $\overline{r}_{0^\circ}(f, \mathbf{0}) = 7.92 \cdot 10^{-2}$ (b) $\overline{r}_{0^\circ}(f, \boldsymbol{U}) = 1.71 \cdot 10^{-2}$ (c) $\overline{r}_{0^\circ}(f, \mathbf{0}) = 1.22 \cdot 10^{-2}$

Figure 4: Projection residual of 4a: the MP-reconstruction, 4b: the $\text{DYN}_{\text{Shear}}$-reconstruction, 4c the GT-reconstruction.

Table 2: Summary of the main metrics

Reconstruction method	$\overline{r}(f, \boldsymbol{U})$	$\overline{\boldsymbol{R}}(\boldsymbol{U})$, $\overline{\boldsymbol{R}}(\boldsymbol{U}_x)$, $\overline{\boldsymbol{R}}(\boldsymbol{U}_y)$	$\overline{\boldsymbol{R}}(f, \boldsymbol{U})$
MP-reconstruction	$14.8 \cdot 10^{-2}$	5.575, 5.423, 1.350	$2.15 \cdot 10^{-2}$
2D warped reconstruction	$11.8 \cdot 10^{-2}$	NA	$2.48 \cdot 10^{-2}$
DYN_{RBM}-reconstruction	$4.74 \cdot 10^{-2}$	1.452, 0.701, 1.333	$1.16 \cdot 10^{-2}$
$\text{DYN}_{\text{Shear}}$-reconstruction	$2.21 \cdot 10^{-2}$	0.147, 0.071, 0.135	$1.05 \cdot 10^{-2}$
MC_{GT}-reconstruction	$2.28 \cdot 10^{-2}$	0, 0, 0	$1.02 \cdot 10^{-2}$
GT-reconstruction	$1.24 \cdot 10^{-2}$	NA	0

$\text{DYN}_{\text{Shear}}$-reconstruction mean residual error is only 124% higher, hence a reduction in average of 1539%. This speaks for a good reconstruction performance and an additional confirmation is that all the 30 reconstructions are very similar in the areas of interest and look very much like figures 6d1, 6d2 and 6d3. In addition, the average difference between the ground truth displacement field and the corrected displacement field is of 0.183 mm (1.83 voxels). This difference decomposes into merely 0.085 mm in the x-axis and 0.168 mm in the y-axis. In comparison, the average initial mismatch is of 5.345 mm (53.45 voxels), decomposed in 5.224 mm in the x-axis and 1.243 mm in the y-axis.

Furthermore, a visualization of the algebraic mean estimation error $\overline{\Delta}$ of the degrees of freedom for each configuration is presented in figure 7. There, an error below one voxel can be observed for the x-axis RBM translations with an uncertainty σ_Δ being relatively constant with the angular position of the source. For y-translations and the associated rotations, the average error is higher and may reach up to 4 voxels. There, the uncertainty seems to increase with the distance to the

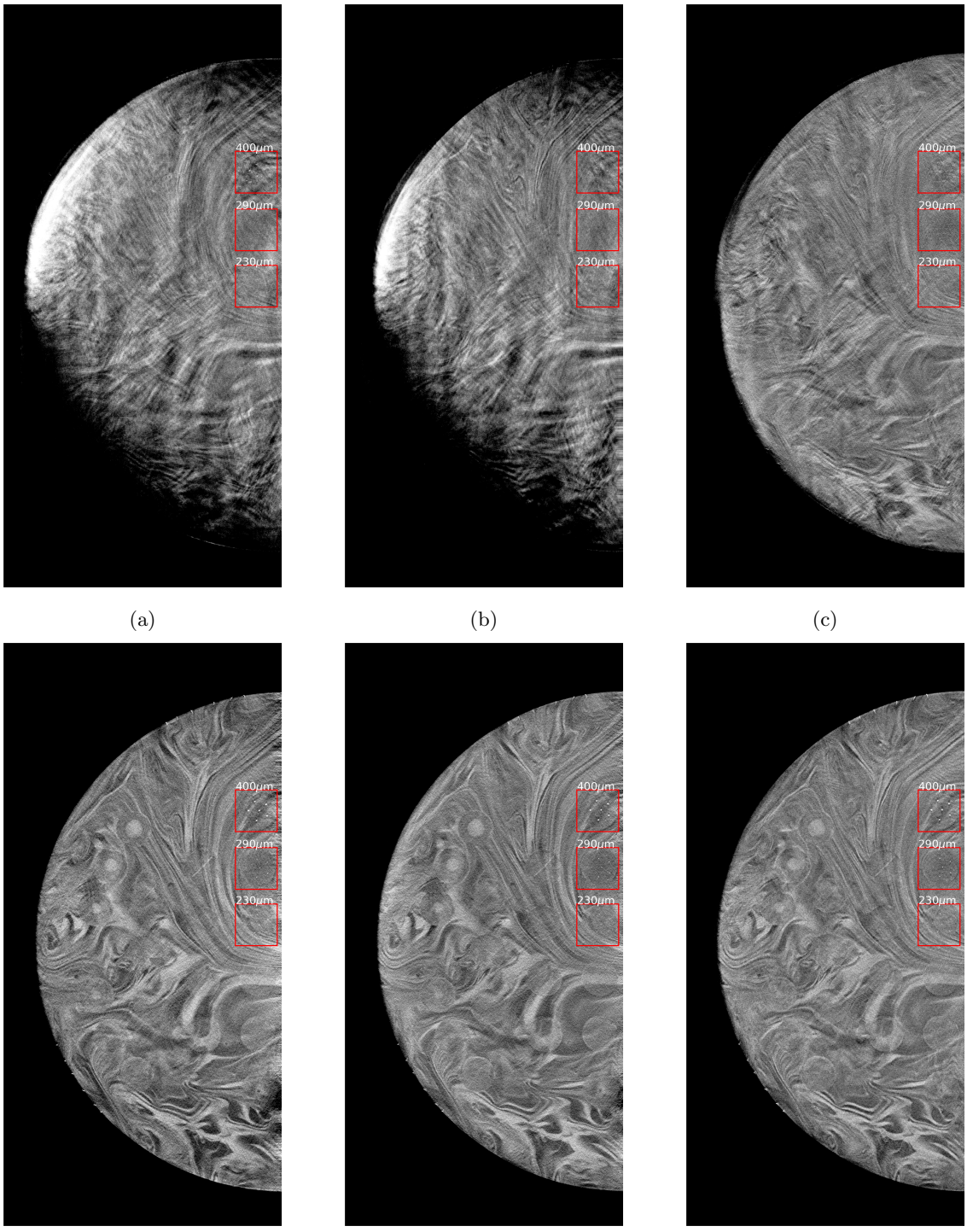

Figure 5: Comparison of reconstruction slices of size 100×200 mm^2 at height $z = 6$ mm of: (5a) Motion polluted, (5b) 2D corrected projections, (5c) RBM 3D correction, (5d) Shear 3D correction, (5e) volume with measured ground truth and (5f) Ground truth static volume.

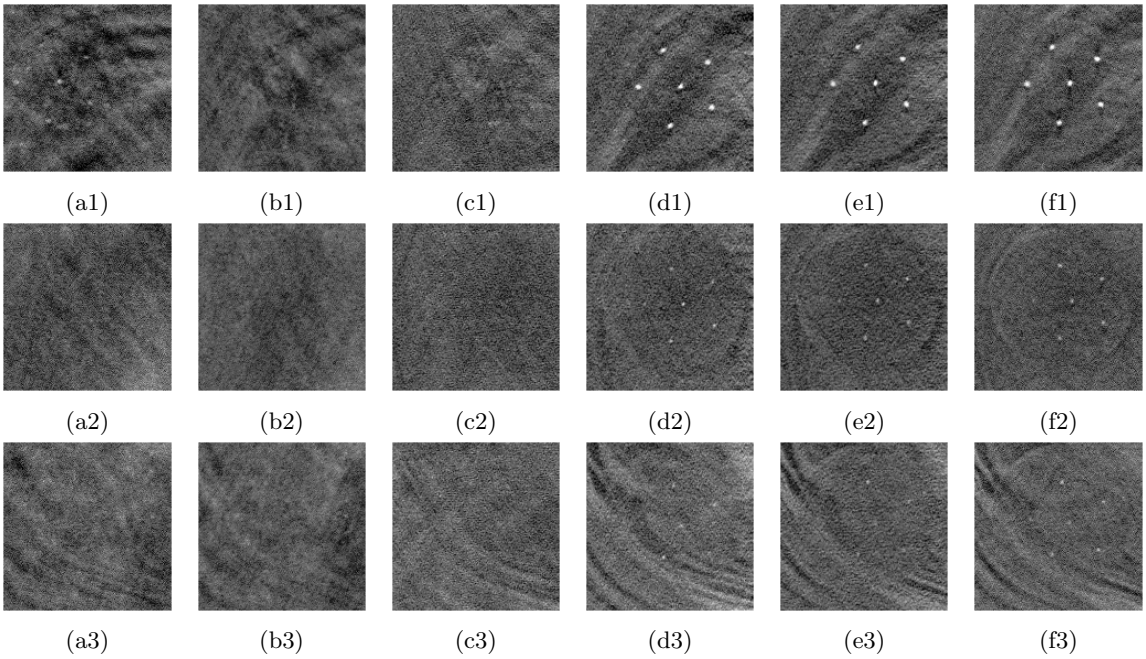

Figure 6: Comparison of the reconstruction of calcifications of different sizes. All figures are of size 15.2×15.2 mm^2 at height $z = 6$ mm. Figures (6a1), (6b1), (6c1), (6d1), (6e1), and (6f1) show the results on calcifications of size 400 µm ordered as follows: motion polluted, 2D corrected, RBM3D corrected, Shear3D, ground truth corrected and ground truth. Figures (6a2), (6b2), (6c2), (6d2), (6e2), and (6f2) refer to 290 µm calcifications and figures (6a3), (6b3), (6c3), (6d3), (6e3), and (6f3) to 230 µm calcifications.

reference angular position (0°) as is particularly visible in the rotation of the middle slab.

Regarding image quality, an assessment of the central microcalcification of each of the three clusters shown in figure 5 by computing the sharpness s. [5] As a result, the average sharpness $\overline{s}$ and the standard deviation σ_s are reported in table 3 for the three clusters of the MP-, $\text{DYN}_{\text{Shear}}$- and GT-reconstructions.

Table 3: Average sharpness comparison for 3 microcalcification clusters $\overline{s} \cdot 10^3$ $(\sigma_s \cdot 10^3)$

Reconstruction method	400μm	290μm	230μm
MP-reconstruction	4.2(0.9)	2.4(0.3)	2.5(0.4)
$\text{DYN}_{\text{Shear}}$-reconstruction	19.8(1.8)	7.9(1.0)	4.1(0.4)
GT-reconstruction	21.9(0)	8.9(0)	3.9(0)

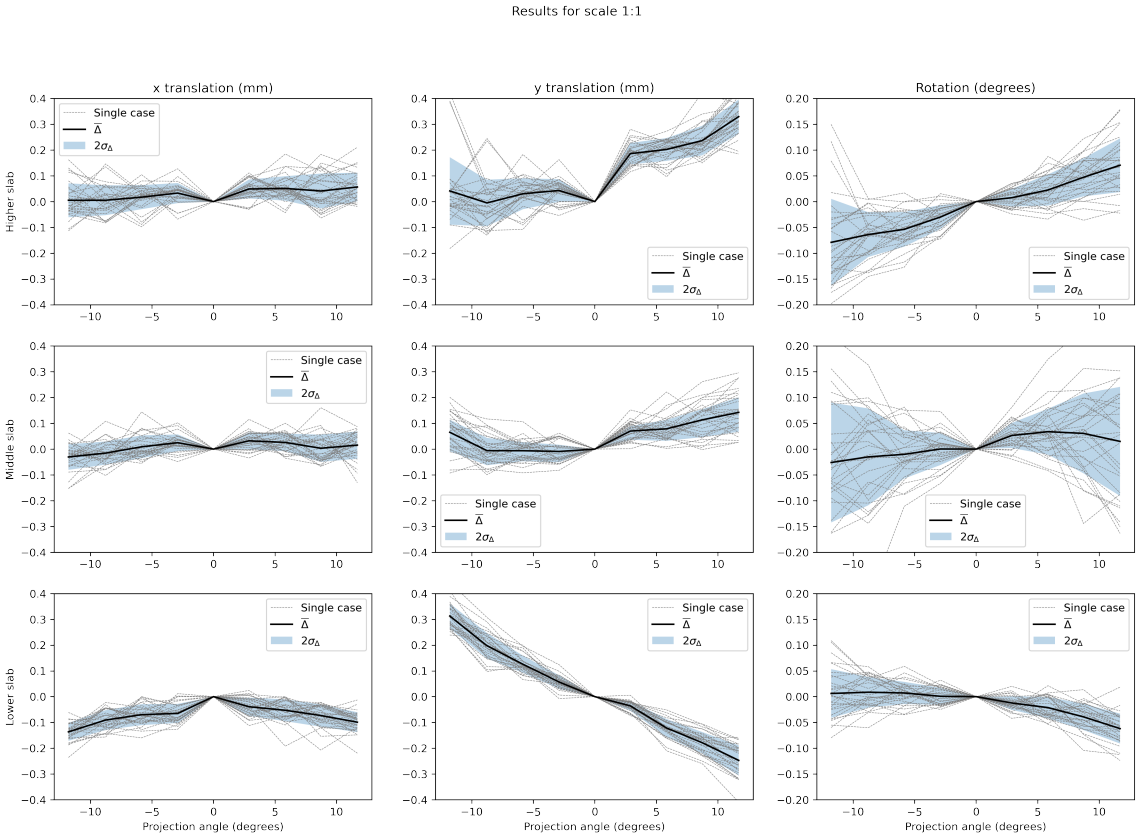

Figure 7: Statistical analysis of the difference to ground truth for 30 motion-pollution combinations.

5. Discussion

The comparison presented in the previous section shows that the dynamic correction workflow described in this paper is able to increase the consistency of the solution with respect to the problem presented in (4), to match the identification of a ground truth displacement with an average precision of 1.3 voxels and to improve the visibility of clinical features.

It is to be noted that the multiscale approach is still an empirical choice that was selected to increase the convergence rate towards the known the ground truth. Indeed, the variance of the Gaussian filter in the downscaled projections must be of the same order of magnitude as the amplitude of the displacement left to estimate. For this purpose, one should have an upfront idea of what the motion amplitude is and select scales so that the condition on $\delta \boldsymbol{U}$ is satisfied at every time point. A more automatic definition of the value of the new scale and regularization intensity should be defined with the help of experience on a greater number of cases. Nonetheless, the selected values for the scaling and regularization strategies were able to lead to a successful identification

for all 30 configurations tested and are thus deemed reasonably robust.

However, the linear drift on the identification of the y translation components shown in figures 3, and 7 is due to the under-determined equation system inherent of tomosynthesis which uncovers an underlining correlation between y and z motions that can not be entirely resolved. In fact, in spite of freezing the vertical degrees of freedom in the shape function basis $\mathbf{\Phi}$ — which only allows for in-plane RBMs — particular y translations are still able to represent a vertical displacement. For instance, let A and B be two points at different heights z_a and z_b in the source motion plane. Then if B moves along the y axis such that it intersects all rays that run from the source to point A at each time step, the reconstruction cannot distinguish between a static point (A) and a moving point (B). In addition, improper calibration of the imaging system may also lead to this kind of systematic bias. As a result, the signal from the lower plate has been reconstructed at a different height than in the static volume (1 mm higher) even though this is hardly perceptible in the volume itself. Hence, more clinically-relevant strategies may be envisioned while adapting the pipeline for a specific application. For instance, temporal regularization of the deformation field could ensure the continuity and smoothness of the motion with respect to the projection sampling.

Then, although the DYN_{RBM}-reconstruction [18] and 2D-reconstruction [37] techniques are used in the literature for motion compensation, they are usually applied on CT datasets to correct for simpler and smaller motions. Hence, their impact is insufficient to correct for the shear motion. This is visible in table 2 as well as in the visual comparison in figures (5b) (resp. (5c)) and (6b1) (resp. (6c1)). The reason is that both cited methods do not cover the complexity of the kinematics induced in the present experimental setup. Nonetheless, it is to be noted that the 2D-reconstruction does resolve the two largest calcification clusters (the ones where tie points were selected), but everything around these details is too corrupted for any clinical use. Perhaps, these methods could be used as an initial guess of the motion estimation to speed up the dynamic reconstruction process, as the routine described in algorithm 1 requires multiple iterations to converge that are computationally more expensive than the standard reconstruction process.

In addition, while the displacements during the acquisition were considerably larger than the ones usually measured during a DBT acquisition (around 1–2 mm, [47, 59]), multiscale approaches in both the reconstruction and regularization processes enabled to achieve artifact removal, which would not have been possible if starting from the original projection scale. Figure 7 shows that the identification in the x-axis has a bias which is inferior 0.1 mm and in the y-axis to 0.4 mm. Eventually, the combination of the final deformation field shows an average precision of 0.183 mm which is the same order of magnitude than a voxel. Besides, the precision in the x-axis is of 0.085 mm which is below the voxel size and most of the error comes from the y-axis (0.168 mm), which is expected following the previous discussion about the under-determined equation system. The ability to correct such large motions at the level of a single voxel is thereby an excellent opportunity to reduce the number of retake acquisitions. While the MP-reconstruction shown in figures (5a) and (6a1) present very blurred texture and a dense cluster of fuzzy microcalcifications,

figure (6d1) enables clinicians to effectively detect and assess the presence, the size and the type of microcalcifications. Furthermore, computing the sharpness around the central microcalcification of all three clusters for 30 cases shows that there is a significant 3-fold improvement from the MP-reconstruction to the $\text{DYN}_{\text{Shear}}$-reconstruction. In fact, the sharpness of the corrected image is of the same order of magnitude as the original GT-reconstruction. In addition, masses (in the outer part of the phantom) and fibers are equally visible in figure 5d which highlights the advantage with respect to a 2D-based correction as in figure 5b. The relevance of this results is capital since the two images may lead to different diagnoses or treatments. Overall, the reason why the $\text{DYN}_{\text{Shear}}$-reconstruction proposed here works better than the DYN_{RBM}- and 2D-reconstructions is that it provides an accurate description of the available kinematics thanks to the function basis $\mathbf{\Phi}$. This comes however with the burden of selecting a basis of shape functions that encapsulates the underlying motion of the volume while limiting the number of degrees of freedom. In this respect, the case treated here is simple to model (plate-wise RBMs), but modeling actual patient's motion efficiently will be a critical challenge for the transfer to the clinical environment and highly depends on the targeted medical application. Options to describe the kinematics include splines, [58] *a priori* mechanical models of the imaged body part [38] or finite element meshing [28].

Additionally, it is essential to remember that the whole dynamic reconstruction framework is driven by the projection residuals and the motion estimation is limited by the discrepancies between the physical setup and projection model. In particular, a significant difference between CT and DTS reconstruction is that in DTS the resolution in the z-axis is usually higher than the one theoretically achievable since the number of reconstructed planes is larger than the number of acquired radiographs. Hence, the reconstruction problem is ill-posed and requires the introduction of additional constraints to direct the optimization towards an acceptable solution. Since none of these constraints are sufficient to fully condition the problem, an additional, intrinsic, regularization of the SIRT algorithm is to be expected and further development should be held in that direction. Similarly, it is important to control all relevant parameters such as *detector noise*, *flatfield correction*, *source positioning uncertainties*, *non-linear absorption*... and ensure that their impact remains negligible in front of the one of patient-motion. If not, other discrepancy causes could falsely be explained as patient's motion and corrupt the dynamic reconstruction. While here little optimization of the reconstruction process was done (except from the positive constraint on the reconstructed volume) it is likely that any additional reconstruction improvement such as assumptions on discrete phases reconstruction [4], total variation (TV) regularization, [49] or beam hardening correction [10, 51] will contribute to the dynamic pipeline improvement. This is also true when deciding what kinematic model is used for the motion estimation and any prior knowledge of the motion that may help to constrain the ill-posed problem can be transparently implemented in the framework.

6. Conclusions

The present work aims at improving the tomosynthesis reconstruction of clinical images by estimating patient's motion from a single series of motion-polluted projections and performing a motion-corrected reconstruction. The process is built on 1) a motion-compensation reconstruction technique derived from the SIRT algorithm and 2) motion estimation based on the P-DVC formalism. In addition, an image multiresolution approach is exploited to ensure the validity of the Taylor-expansion at any given step and a progressively vanishing Tikhonov regularization is applied to gradually increment the number of degrees of freedom used for the motion estimation. The workflow has been validated on the BR3D model 020 (CIRS Inc., Norfolk, VA, USA) breast imaging phantom in the case of "shear" motion and has provided considerable improvement with respect to all evaluation metrics described in paragraph 3.5. More specifically, it has demonstrated the ability to recover clinical features and decreased the root mean error with the GT-reconstruction by 59.9%. In addition, the measurement of the deformation field has an average precision of 0.183 mm (x: 0.085 mm, y:0.168 mm), which allows for corrections of the order of magnitude of the voxel size.

Thanks to the shape function basis $\mathbf{\Phi}$ the proposed 3D motion identification technique can be adapted to any kind of kinematics. This includes non-periodic motions, and provides the flexibility to be tailored to any specific application requirements. While estimation of non-rigid motions was not tested in the current work, the proposed framework is able to represent the patient's motion if given enough degrees of freedom. Thus, future work will focus on the transfer of this technology to the clinical environment by defining suited kinematic models and incorporating additional application-dependent constraints to improve the reconstruction process.

Acknowledgement

M. B. acknowledges the support of a CIFRE Ph.D. grant from ANRT # 2021-1460, and GE HealthCare.

References

[1] Adelson, E. H., Burt, P. J., Anderson, C. H., Ogden, J. M. and Bergen, J. R. [1984], 'Pyramid methods in image processing.', *RCA engineer* **29**(6), 33–41.

[2] Andersen, A. H. and Kak, A. C. [1984], 'Simultaneous Algebraic Reconstruction Technique (SART): A superior implementation of the ART algorithm', *Ultrasonic Imaging* **6**(1), 81–94.

[3] Baratella, E., Quaia, E., Crimì, F., Minelli, P., Cioffi, V., Ruaro, B. and Cova, M. A. [2023], 'Digital tomosynthesis as a problem-solving technique to confirm or exclude pulmonary lesions in hidden areas of the chest', *Diagnostics* **13**, 1010.

[4] Batenburg, K. J. and Sijbers, J. [2011], 'DART: a practical reconstruction algorithm for discrete tomography.', *IEEE transactions on image processing : a publication of the IEEE Signal Processing Society* **20**(9), 2542–2553.

[5] Batten, C. F., Holburn, D. M., Breton, B. C. and Caldwell, N. H. M. [2001], 'Sharpness search algorithms for automatic focusing in the scanning electron microscope', *Scanning* **23**(2), 112–113.

[6] Becher, H., Schlüter, M., Mathey, D. G., Bleifeld, W., Klotz, E., Haaker, P., Llnde, R. and Weiss, H. [1985], 'Coronary angiography with flashing tomosynthesis', *European Heart Journal* **6**, 399–408.

[7] Behling, R. [2021], 'On a new multi-source X-ray tube concept for minimizing imaging time in digital breast tomosynthesis', *Physica Medica* **88**, 20–22.

[8] Berger, M., Müller, K., Aichert, A., Unberath, M., Thies, J., Choi, J. H., Fahrig, R. and Maier, A. [2016], 'Marker-free motion correction in weight-bearing cone-beam CT of the knee joint', *Medical Physics* **43**, 1235–1248.

[9] Blum, A., Noël, A., Regent, D., Villani, N., Gillet, R. and Teixeira, P. G. [2018], 'Tomosynthesis in musculoskeletal pathology', *Diagnostic and Interventional Imaging* **99**(7-8), 423–441.

[10] Bustamante, V. M., Nagy, J. G., Feng, S. S. and Sechopoulos, I. [2013], 'Iterative breast tomosynthesis image reconstruction', *SIAM Journal on Scientific Computing* **35**(5), S192–S208.

[11] Chee, G., O'Connell, D., Yang, Y. M., Singhrao, K., Low, D. A. and Lewis, J. H. [2019], 'McSART: An iterative model-based, motion-compensated SART algorithm for CBCT reconstruction', *Physics in Medicine and Biology* **64**(9), 095013.

[12] Chen, G. T., Kung, J. H. and Beaudette, K. P. [2004], 'Artifacts in computed tomography scanning of moving objects', *Seminars in Radiation Oncology* **14**(1), 14–26.

[13] Choi, J. H., Fahrig, R., Keil, A., Besier, T. F., Pal, S., McWalter, E. J., Beaupré, G. S. and Maier, A. [2013], 'Fiducial marker-based correction for involuntary motion in weight-bearing C-arm CT scanning of knees. Part I. numerical model-based optimization', *Medical Physics* **40**(9), 091905.

[14] Choi, J. H., Maier, A., Keil, A., Pal, S., McWalter, E. J., Beaupré, G. S., Gold, G. E. and Fahrig, R. [2014], 'Fiducial marker-based correction for involuntary motion in weight-bearing C-arm CT scanning of knees. II. experiment', *Medical Physics* **41**(6), 061902.

[15] CIRS [2023], 'Mammography phantoms catalogue', https://www.cirsinc.com/products/?filters=modality%5B328%5D.

[16] Dobbins III, J. T. [2009], 'Tomosynthesis imaging: At a translational crossroads', *Medical Physics* **36**(6), 1956–1967.

[17] Dobbins III, J. T. and Godfrey, D. J. [2003], 'Digital X-ray tomosynthesis: Current state-of-the-art and clinical potential', *Physics in Medicine and Biology* **48**(19), R65–R106.

[18] Eldib, M. E., Hegazy, M. A., Cho, M. H., Cho, M. H. and Lee, S. Y. [2018], 'A motion artifact reduction method for dental CT based on subpixel-resolution image registration of projection data', *Computers in Biology and Medicine* **103**, 232–243.

[19] Feldkamp, L. A., Davis, L. C. and Kress, J. W. [1984], 'Practical cone-beam algorithm', *Journal of the Optical Society of America A* **1**(6), 612–619.

[20] Ferrari, A., Bertolaccini, L., Solli, P., Salvia, P. O. D. and Scaradozzi, D. [2018], 'Digital chest tomosynthesis: the 2017 updated review of an emerging application', *Annals of Translational Medicine* **6**(5), 91.

[21] Geiser, W. R., Einstein, S. A. and Yang, W. T. [2018], 'Artifacts in digital breast tomosynthesis', *American Journal of Roentgenology* **211**(4), 926–932.

[22] Gilbert, P. [1972], 'Iterative methods for the three-dimensional reconstruction of an object from projections', *Journal of Theoretical Biology* **36**(1), 105–117.

[23] Gordon, R., Bender, R. and Herman, G. T. [1970], 'Algebraic Reconstruction Techniques (ART) for three-dimensional electron microscopy and X-ray photography', *Journal of Theoretical Biology* **29**(3), 471–481.

[24] Haas, B. M., Kalra, V., Geisel, J., Raghu, M., Durand, M. and Philpotts, L. E. [2013], 'Comparison of tomosynthesis plus digital mammography and digital mammography alone for breast cancer screening', *Radiology* **269**(3), 694–700.

[25] Huang, X., Zhang, Y., Chen, L. and Wang, J. [2020], 'U-net-based deformation vector field estimation for motion-compensated 4D-CBCT reconstruction', *Medical Physics* **47**(7), 3000–3012.

[26] Jailin, C., Buffière, J. Y., Hild, F., Poncelet, M. and Roux, S. [2017], 'On the use of flat-fields for tomographic reconstruction', *Journal of Synchrotron Radiation* **24**(1), 220–231.

[27] Jailin, C. and Roux, S. [2018], 'Dynamic tomographic reconstruction of deforming volumes', *Materials* **11**(8), 1395.

[28] Jailin, C., Roux, S., Sarrut, D. and Rit, S. [2021], 'Projection-based dynamic tomography', *Physics in Medicine and Biology* **66**(21).

[29] Johnsson, Å. A., Vikgren, J., Svalkvist, A., Zachrisson, S., Flinck, A., Boijsen, M., Kheddache, S., Månsson, L. G. and Båth, M. [2010], 'Overview of two years of clinical experience of chest tomosynthesis at Sahlgrenska university hospital', *Radiation Protection Dosimetry* **139**(1-3), 124–129.

[30] Kak, A. C. and Slaney, M. [2002], 'Principles of computerized tomographic imaging', *Medical Physics* **29**(1).

[31] Lai, Y. C., Ray, K. M., Mainprize, J. G., Kelil, T. and Joe, B. N. [2020], 'Digital breast tomosynthesis: Technique and common artifacts', *Journal of Breast Imaging* **2**(6), 615–628.

[32] Langer, S. G., Graner, B. D., Schueler, B. A., Fetterly, K. A., Kofler, J. M., Mandrekar, J. N. and Bartholmai, B. J. [2016], 'Sensitivity of thoracic Digital Tomosynthesis (DTS) for the identification of lung nodules', *Journal of Digital Imaging* **29**(1).

[33] Lauritsch, G., Boese, J., Wigström, L., Kemeth, H. and Fahrig, R. [2006], 'Towards cardiac C-arm computed tomography', *IEEE Transactions on Medical Imaging* **25**(7), 922–934.

[34] Li, T., Koong, A. and Xing, L. [2007], 'Enhanced 4D cone-beam CT with inter-phase motion model', *Medical Physics* **34**(9), 3688–3695.

[35] Li, T., Zhang, M., Qi, W., Asma, E. and Qi, J. [2022], 'Deep learning based joint PET image reconstruction and motion estimation', *IEEE Transactions on Medical Imaging* **41**(5).

[36] Li, T., Zhang, X., Xie, Z., Shi, H., Cherry, S., Badawi, R. and Qi, J. [2021], 'Total-body parametric reconstruction with deep learning-based data-driven motion compensation', *Journal of Nuclear Medicine* **62**(supplement 1), 60.

[37] Marchant, T. E., Price, G. J., Matuszewski, B. J. and Moore, C. J. [2011], 'Reduction of motion artefacts in on-board cone beam CT by warping of projection images', *British Journal of Radiology* **84**(999), 251–264.

[38] McClelland, J. R., Modat, M., Arridge, S., Grimes, H., D'Souza, D., Thomas, D., Connell, D. O., Low, D. A., Kaza, E., Collins, D. J., Leach, M. O. and Hawkes, D. J. [2017], 'A generalized framework unifying image registration and respiratory motion models and incorporating image reconstruction, for partial image data or full images', *Physics in Medicine and Biology* **62**(11), 4273–4292.

[39] McKinnon, G. C. and Bates, R. H. [1981], 'Towards imaging the beating heart usefully with a conventional CT scanner', *IEEE Transactions on Biomedical Engineering* **BME-28**(2), 123–127.

[40] Nassi, M., Brody, W. R., Medoff, B. P. and Macovski, A. [1982], 'Iterative reconstruction—reprojection: an algorithm for limited data cardiac—computed tomography', *IEEE Transactions on Biomedical Engineering* **BME-29**(5).

[41] Nieuwenhove, V. V., Beenhouwer, J. D., Vlassenbroeck, J., Brennan, M. and Sijbers, J. [2017], 'MoVIT: a tomographic reconstruction framework for 4D-CT', *Optics express* **25**(16), 19236–19250.

[42] Osman, M. M., Cohade, C., Nakamoto, Y., Marshall, L. T., Leal, J. P. and Wahl, R. L. [2003], 'Clinically significant inaccurate localization of lesions with PET/CT: frequency in 300 patients.', *Journal of nuclear medicine : official publication, Society of Nuclear Medicine* **44**(2), 240–243.

[43] Palma, G. J. J., Espino, J. C., Klausz, R. and Iordache, R. [2021], 'Method and system for motion assessment and correction in digital breast tomosynthesis', (US-11660061-B2).

[44] Pauchard, Y., Ayres, F. J. and Boyd, S. K. [2011], 'Automated quantification of three-dimensional subject motion to monitor image quality in high-resolution peripheral quantitative computed tomography', *Physics in Medicine and Biology* **56**(20), 6523–6543.

[45] Qian, X., Tucker, A., Gidcumb, E., Shan, J., Yang, G., Calderon-Colon, X., Sultana, S., Lu, J., Zhou, O., Spronk, D., Sprenger, F., Zhang, Y., Kennedy, D., Farbizio, T. and Jing, Z. [2012], 'High resolution stationary digital breast tomosynthesis using distributed carbon nanotube x-ray source array', *Medical Physics* **39**(4), 2090–9.

[46] Quillent, A., Bismuth, V. J., Bloch, I., Kervazo, C. and Ladjal, S. [2023], A deep learning method trained on synthetic data for digital breast tomosynthesis reconstruction, *in* 'Medical Imaging with Deep Learning'.

[47] Ren, B., Zhang, Y., Ruth, C., Smith, A., Niklason, L., Tao, Z. and Jing, Z. [2011], Automatic patient motion detection in digital breast tomosynthesis, Vol. 7961, p. 79615F.

[48] Rit, S., Sarrut, D. and Desbat, L. [2009], 'Comparison of analytic and algebraic methods for motion-compensated cone-beam CT reconstruction of the thorax', *IEEE Transactions on Medical Imaging* **28**(10), 1513–1525.

[49] Seyyedi, S. and Yildirim, I. [2014], '3D digital breast tomosynthesis image reconstruction using anisotropic total variation minimization', *2014 36th Annual International Conference of the IEEE Engineering in Medicine and Biology Society, EMBC 2014* pp. 6052–6055.

[50] Sharpe, R. E., Venkataraman, S., Phillips, J., Dialani, V., Fein-Zachary, V. J., Prakash, S., Slanetz, P. J. and Mehta, T. S. [2016], 'Increased cancer detection rate and variations in the recall rate resulting from implementation of 3D digital breast tomosynthesis into a population-based screening program', *Radiology* **278**(3), 698–706.

[51] Six, N., Beenhouwer, J. D. and Sijbers, J. [2019], 'poly-DART: A discrete algebraic reconstruction technique for polychromatic X-ray CT', *Optics Express* **27**(23), 33670–33682.

[52] Skaane, P., Bandos, A. I., Gullien, R., Eben, E. B., Ekseth, U., Haakenaasen, U., Izadi, M., Jebsen, I. N., Jahr, G., Krager, M., Niklason, L. T., Hofvind, S. and Gur, D. [2013], 'Comparison of digital mammography alone and digital mammography plus tomosynthesis in a population-based screening program', *Radiology* **267**(1), 47–56.

[53] Van Eyndhoven, G., Sijbers, J. and Batenburg, J. [2012], Combined motion estimation and reconstruction in tomography, *in* A. Fusiello, V. Murino and R. Cucchiara, eds, 'Computer Vision – ECCV 2012. Workshops and Demonstrations', Springer Berlin Heidelberg, Berlin, Heidelberg, pp. 12–21.

[54] Vikgren, J., Zachrisson, S., Svalkvist, A., Johnsson, Å. A., Boijsen, M., Flinck, A., Kheddache, S. and Båth, M. [2008], 'Comparison of chest tomosynthesis and chest radiography for detection of pulmonary nodules: Human observer study of clinical cases', *Radiology* **249**(3), 1034–1041.

[55] Wang, G. and Vannier, M. W. [1995], 'Preliminary study on helical CT algorithms for patient motion estimation and compensation', *IEEE Transactions on Medical Imaging* **14**(2), 205–211.

[56] Wang, J. and Gu, X. [2013], 'Simultaneous Motion Estimation and Image Reconstruction (SMEIR) for 4D cone-beam CT', *IEEE Nuclear Science Symposium Conference Record* p. 101912.

[57] Yu, H., Wei, Y., Hsieh, J. and Wang, G. [2006], 'Data consistency based translational motion artifact reduction in fan-beam CT', *IEEE Transactions on Medical Imaging* **25**(6), 249–260.

[58] Zeng, R., Fessler, J. A. and Balter, J. M. [2005], 'Respiratory motion estimation from slowly rotating X-ray projections: Theory and simulation', *Medical Physics* **32**(4), 984–991.

[59] Zeng, R., Jia, C., Akhlaghi, N., Torkaman, M., Garra, B., Alton, K., Brem, R., Ahmed, T., Kaczmarek, R. and Myers, K. J. [2018], Measuring breast motion at multiple DBT compression levels using ultrasound speckle-tracking techniques, *in* E. A. Krupinski, ed., '14th International Workshop on Breast Imaging (IWBI 2018)', Vol. 10718, International Society for Optics and Photonics, SPIE, p. 107180L.

[60] Zhao, C., Herbst, M., Weber, T., Vogt, S., Ritschl, L., Kappler, S., Siewerdsen, J. H. and Zbijewski, W. [2021], Image-domain cardiac motion compensation in multidirectional digital chest tomosynthesis.